Thermochemical conversion of carbon dioxide by reverse water-gas shift chemical looping using supported perovskite oxides

Bryan J. Hare[1]*, Debtanu Maiti*[1]*, Swetha Ramani*[2]*, Adela E. Ramos*[1]*,*
Venkat R. Bhethanabotla[1,2]**, and John N. Kuhn*[1,2]***

[1] Department of Chemical & Biomolecular Engineering
[2] Department of Chemistry
University of South Florida (USF), Tampa, FL 33620, USA
Email: jnkuhn@usf.edu; bhethana@usf.edu

Abstract

Perovskite-type oxides show clear potential for thermochemical solar-driven CO_2 conversion. These materials exhibit the exact characteristics (e.g., structural endurance and high oxygen redox capacity and exchange kinetics) required by the low temperature reverse water-gas shift chemical looping process. In this study, the $La_{0.75}Sr_{0.25}FeO_3$ (LSF) perovskite oxide was combined with various supports, including popular redox materials CeO_2 and ZrO_2 along with more abundant alternatives such as Al_2O_3, SiO_2, and TiO_2, for potential application at industrial scale. Supporting LSF on SiO_2 by 25% mass resulted in the largest increase of 150% in CO yields relative to unsupported perovskite after reduction at 600 °C. This is a result of significantly reduced perovskite oxide particle size confirmed by SEM/TEM imaging and crystallite size from Scherrer analyses of XRD patterns. Due to solid-state reactions, minor secondary phases were observed at the LSF:support interface when using SiO_2 or TiO_2. Oxygen vacancy formation occurred only on the perovskite oxide phase, as suggested by low temperature experiments and consistent with density functional theory calculations. The role of each metal oxide support towards suppressing or enhancing the CO_2 conversion is elucidated. Through utilization of SiO_2 as support, the reverse water-gas shift chemical looping process using perovskite-based composites was significantly improved.

Key Words: CO_2 conversion; syngas production; chemical looping; perovskite oxide; defect energetics; catalyst support

1.0 Introduction

Energy-based processes that utilize CO_2 as a feedstock are crucial for realigning the carbon cycle. Even as the modern world adopts alternatives (wind, solar, etc.), tangible carbon-based fuel will still be required for transportation. While the use of renewable energy was estimated to be only 10.5% of the total U.S. energy consumption in 2016 [1], the U.S. Energy Information Administration reported about 5.2 GT of national CO_2 emissions the same year [2]. These considerations have garnered interest throughout the scientific community to develop processes for sustainable CO_2 reduction, energy storage, and generation of economically valuable products. As a major component of synthesis gas, CO provides a flexible basis for renewable fuel production and energy storage. Following the reduction of CO_2, the resulting CO can be used in the subsequent formation of various energy-dense molecules including methanol, olefins, large hydrocarbons, and higher order alcohols [3-5], that form the backbone of this energy market [6]. Therefore, it is crucial to identify an efficient catalytic process and material that can feasibly convert CO_2 into liquid fuel intermediates.

Reverse water-gas shift chemical looping (RWGS-CL) is a process capable of converting vast quantities of CO_2 not only to reduce net emissions, but also provide an economical supply of syngas [7-9]. Renewable H_2 (obtained from solar-driven H_2O splitting [10]) is initially used to reduce a metal oxide and generate oxygen vacancies (Reaction I) to create non-stoichiometric oxides ($MO_{x-\delta}$) and active sites for CO_2 reduction. The oxygen deficient material is then utilized for the subsequent conversion of CO_2 to CO (Reaction II). Through cyclic repetition of these two steps, RWGS-CL (Reaction I+II) may be operated perpetually as a 100% CO selective intermediate process for renewable fuel production. Under isothermal conditions at temperatures

of 450-750 °C and ambient pressure [7, 11, 12], the RWGS-CL process was determined to be up to 54% more energy efficient than the traditional RWGS reaction [13]. By maintaining these low temperatures, the solar-to-fuel efficiency of this looping process is expected to surpass that of current technologies [13, 14]. Moreover, this process also circumvents the challenges of side-reactions faced in conventional RWGS. These facts leave the essential step of designing an oxide material that is capable of balancing formation of numerous oxygen vacancies, kinetics for CO_2 activation and oxygen exchange, and lasting through numerous reaction cycles.

$H_2 + MO_x \rightarrow H_2O + MO_{x-\delta}$ (I)

$CO_2 + MO_{x-\delta} \rightarrow CO + MO_x$ (II)

$H_2 + CO_2 \rightarrow H_2O + CO$ (I+II)

Perovskite-type oxides (ABO_3) fit the criteria for generating vast quantities of CO in the RWGS-CL process. With the ability to tailor the lattice and synthesize an infinite array of metal combinations, significant effort has been spent towards fine-tuning the properties of these materials to maximize redox abilities [15, 16]. Perovskites of diverse compositions have been shown to match and even surpass the redox activity of popular redox materials such as CeO_2 in the thermochemical conversion of both CO_2 and H_2O [17-19]. The utilization of perovskites in redox applications is advantageous due to the formation of an oxygen diffusion network throughout the bulk lattice. In the instance of C-O bond cleavage during CO_2 reduction on the catalyst surface, the resulting oxygen atom diffuses into the bulk and reopens the active site. Stable nonstoichiometric perovskites with high concentrations of vacancies typically exhibit higher rates of oxygen self-diffusion [20, 21] as well as stronger CO_2 affinity [12]. The $La_{0.75}Sr_{0.25}FeO_3$ (LSF) perovskite is a profound base material that possesses these traits and consistently demonstrates high activity in the RWGS-CL process [11, 12, 22] and other

applications that depend on its atomic defects [23-27]. However, the true potential of LSF and many other perovskites remains unrecognized due a considerable lack of specific surface area [15]. With emerging solarthermal reactor technology for water-gas shift reactions and thermochemical splitting [28-30], it is crucial to design novel perovskite-based materials that maintain high surface area over long-term use at elevated temperatures. Industrial-scale pellets are often shaped as spheres, cylinders, Raschig rings, and other common variations with an extruded substrate serving as a catalyst support [31-33]. As opposed to using bulk single-phase catalyst pellets, the inclusion of supporting material is necessary to improve perovskite surface area and accelerate oxygen self-diffusion. The speed at which oxygen is exchanged by nonstoichiometric oxides may be modeled with the one-dimensional equation

$$\frac{M_t}{M_\infty} = 1 - \sum_{n=1}^{\infty} \frac{2L^2 \exp(-\frac{b_n^2 Dt}{l^2})}{b_n^2(b_n^2 + L^2 + L)} \quad \ldots\ldots\ldots (1)$$

where M_t is the sample mass at time t, M_∞ is the sample mass at the experiment conclusion and l is the radius. D represents the effective diffusivity of the oxygen vacancy which in this case will depend on the perovskite metallic composition and a thermodynamic proportionality factor [34, 35]. An effective diffusivity coefficient (D) of 2×10^{-7} cm^2/s was obtained for LSF at 600 °C through the interpolation of data obtained by Armstrong et. al [36]. L is the dimensionless ratio lk/D where k is the surface exchange coefficient, given as 10^{-5} cm/s [37]. b_n is the n^{th} positive root of b*tan(b) = L [38]. This phenomenon, illustrated in Fig. 1 with LSF, foreshadows low CO yields and long cycle times if pellets are designed without supporting material able to maintain a high surface to volume ratio for the perovskite phase. Therefore, identifying an optimal material that is proficient in maintaining small catalyst particle sizes and, as a result, enhancing the CO_2 conversion by LSF and other perovskite oxides remains imperative.

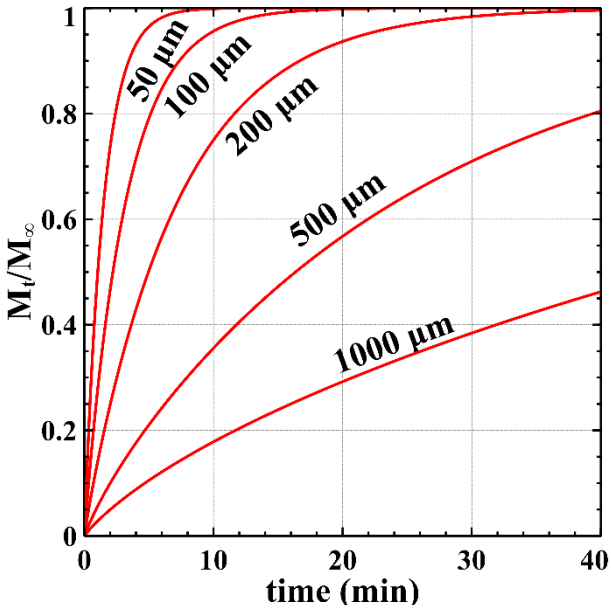

Fig. 1. Change in nonstoichiometric LSF mass over time with different particle sizes. The time required for vacancies to replenish decreases with particle size as calculated by Eqn 1 ($D = 2 \times 10^{-7}$ cm^2/s).

By focusing strictly on oxide supports, there lies the potential to expand the perovskite oxygen network. CeO_2 for instance is a popular material for its high extent of oxygen vacancy formation and replenishment in various redox applications [39-46]. ZrO_2 has also sufficed as both an active catalyst and efficient catalyst support [47, 48] and may even introduce additional oxygen vacancies when Zr is doped into the active phase [49, 50]. While catalyst size reduction was already demonstrated using these supports [51], large-scale CO_2 utilization may require a lower cost alternative. A few earth-abundant examples include Al_2O_3, SiO_2, and TiO_2, each of which have been previously tested as supports for assorted types of catalysts [52-61].

This study concentrated on the use of various catalyst supports for reducing complex oxide particle size, and therefore, increasing CO formation in the RWGS-CL process, enabling

large scale industrial implementation. While focus was given to LSF, the ideal support should suffice for any thermodynamically stable perovskite capable of sustaining vacancies without deterioration. LSF was supported on popular materials such as CeO_2 and ZrO_2 along with more abundant alternatives including Al_2O_3, SiO_2, and TiO_2. These composites were tested in temperature-programed experiments with H_2 and CO_2 to observe distinctions in redox activity. These findings were backed by density functional theory (DFT) based calculations regarding vacancy formation energies. Samples were intensively characterized with X-ray diffraction (XRD), scanning electron microscopy (SEM), and transmission electron microscopy (TEM) to decipher the crystallographic reasoning behind improved or curtailed CO_2 conversion by perovskites in the RWGS-CL process.

2.0 Experimental

2.1 Composite material synthesis

The perovskite phase was synthesized using the Pechini method [62]. $La(NO_3)_3$ (Alfa Aesar 99.99%), $SrCO_3$ (Aesar 99.994%), and $Fe(NO_3)_3$ (Aldrich ACS grade +98%) were combined in an aqueous solution also consisting of citric acid (CA) as a chelating agent. Continuous stirring at 60 °C ensured mixture homogeneity before ethylene glycol (EG) was added to induce polyesterification and obtain a viscous gel after 7 hr of stirring at 90 °C. The gel was charred at 450 °C for 2 hr and crushed into a fine powder before 6 hr of calcination in air at 950 °C to remove any remaining carbon residue. The A:B:EG:CA molar ratio was maintained, following literature [63], as 1:1:10:40. The resulting catalyst was then combined with CeO_2, ZrO_2, Al_2O_3 (Sigma-Aldrich puriss corundum) , SiO_2(Sigma-Aldrich purum quartz), TiO_2 (Alfa Aesar 99.5% rutile) 25% by mass. Each composite material was grinded and subjected to thermal treatment at 950 °C for 10 hr to ensure strong adhesion of the perovskite phase to the support

particles. CeO_2 and ZrO_2 in particular were acquired by thermolysis of $Ce(NO_3)_3$ (Alfa Aesar 99.5%) and $ZrO(NO_3)_2$ respectively at 600 °C [64]. Given previously reported surface areas of 1.9 and 1.1 m^2/g for LSF and SiO_2-supported LSF respectively [65], the surface areas of all other composites are expected to be less than 5 m^2/g.

2.2 Reaction testing

Temperature-programmed experiments were conducted in a quartz microreactor connected to an online MKS Cirrus mass spectrometer to decipher the reducibility and CO_2 convertibility of each composite. The reactor held about 75 mg of sample during each test and was heated using a Thermo Scientific furnace. A total volumetric flow rate of 50 sccm was utilized for all experiments using ultra-high purity grade gas (Airgas). Temperature-programmed reduction (TPR) experiments were conducted to identify a reduction temperature for all samples that demonstrated notable vacancy formation in any given phase. The temperature was ramped to 950 °C at a rate of 10 °C/min under a 10% H_2 in He (v/v) feed flow. Temperature-programmed oxidation (TPO-CO_2) experiments started with isothermal reduction at 600 °C for 30 min with the aforementioned H_2 feed. Samples were then cooled under inert flow to maintain oxygen vacancies prior to ramping the temperature to 950 °C at a rate of 10 °C/min with 10% CO_2 in He (v/v). H_2O and CO formation were depicted by brief increases in the m/z = 18 and 28 signals, respectively. Numerical analysis and integration resulted in product yields, rates, and corresponding temperatures. Procedures for 8 cycles of isothermal RWGS-CL were replicated from a previous study [65] so post-reaction particle sizes and crystal morphologies may be probed with microscopy.

2.3 Material characterization

Crystal phases were probed using X-ray diffraction (XRD). A Bruker X-Ray Diffractometer with Cu Kα and a wavelength of 0.154 nm was operated at ambient conditions to obtain the crystallographic data. Diffraction patterns ranged from 20 to 80° (2θ°) with a step size of 0.0102° (2θ°) at 1.2 s per step. Normalized data was juxtaposed with literature patterns from X'Pert Highscore Plus software to identify known phases and obtain initial guess for lattice parameters. All three lattice parameters for each phase, along with the cell volume, were simultaneously determined using the minimum mean square error method and unique geometrical formulas relating the parameters to interplanar distance [66]. Each post-calcination and post-experiment sample was accompanied by a Scherrer analysis around the dominant (020) facet. A shape factor of 0.9 sufficed, given the assumption of spherical perovskite particles [66]. These calculations were used to estimate the change in LSF crystallite size throughout the material lifetime. Rietveld refinement using Topas 5 software was performed on the LSF control sample diffraction pattern to ensure the accuracy of the raw data and numerical calculations with atomic coordinates provided by Dann et al. [67].

A Field Emission Scanning electron microscope (SEM), accompanied with energy-dispersive spectroscopy (EDS), was used for precise imaging and elemental analysis of the post-calcination and post-experiment perovskite phases. The Hitachi S800 SEM with EDS attachment was operated with 2 nm resolution at a working distance of 5 mm. High resolution transmission electron microscopy (HRTEM) was carried out using a Tecnai F20 microscope operated at 200 kV. Using a line resolution of 0.102 nm and 26° diffraction angle, the dominant LSF facet was revealed along with that of the supporting material.

2.4 DFT calculations

The oxygen vacancy formation energy of the perovskite oxide and the metal oxide supports (CeO_2, TiO_2, SiO_2, ZrO_2, and Al_2O_3) was obtained through DFT-based calculations using Vienna ab initio Simulation Package (VASP – 5.3.3) [68-70]. Plane wave basis sets were considered throughout the calculations along with generalized gradient approach (GGA) for electron densities. Projector augmented wave (PAW) potentials [71] and Perdew-Burke-Ernzerhof (PBE) [72] variant of exchange correlation was used. A consistent energy cut off of 600 eV was maintained throughout the calculations. The crystal structures of these materials were based on the experimental results as obtained from XRD patterns. The atomic distribution within the crystal lattice was based on the minimum energy configuration as per DFT-calculations. Pure bulk LSF perovskite oxide was modeled by a 2×2×2 supercell comprising of 40 atoms. Monkhorst Pack grid [73] based 4×4×4 k-point mesh was used for the calculations of LSF. For the metal oxides, the k-point mesh was generated according the supercell size in order to maintain a similar k-point grid spacing. The convergence criterion of 0.001eV/atom was used for the ionic relaxations. Once the initial ground state configurations of these materials were obtained through varying cell volume calculations, these were used for subsequent oxygen vacancy calculations. Oxygen atoms were removed to create a consistent oxygen vacancy extent (δ) of 0.125. The resulting oxygen vacancy formation energies as calculated according to the following equation were used to gain insights on the materials' tendency to form oxygen vacancies.

$$E_{vac} = E_{MO_{(x-\delta)}} + \delta \times \frac{n}{2} E_{O_2} - E_{MO_x} \ldots\ldots\ldots (2)$$

E_{MO_x} is the total energy of the pure stoichiometric materials (LSF and the metal oxides), n is the number of unit cells in a supercell, while $E_{MO_{(x-\delta)}}$ is that of the oxygen vacant material and E_{O_2} is

the molecular energy of oxygen. The correction factor for oxygen over-binding error (for PBE functionals) by Wang et al. was considered as well [74].

3.0 Results

3.1 Temperature-programmed experiments

Each composite and LSF individually was subjected to TPR and TPO-CO_2 experiments to identify conversion temperatures and quantify H_2O and CO_2 yields. TPR results (Fig. 2a) suggested oxygen vacancy formation occurred, an important step in initiating the RWGS-CL process. Signal elevation below 700 °C is interpreted as partial reduction of the perovskite phase (ABO_3 to $ABO_{3-\delta}$) while that above 800 °C was confirmed to be decomposition of the perovskite into binary oxides such as FeO (Fig. S1) [65]. Thus, TPR profiles suggested 600 °C is an adequate temperature for creating vacancies and thus active sites for CO_2 conversion. CO

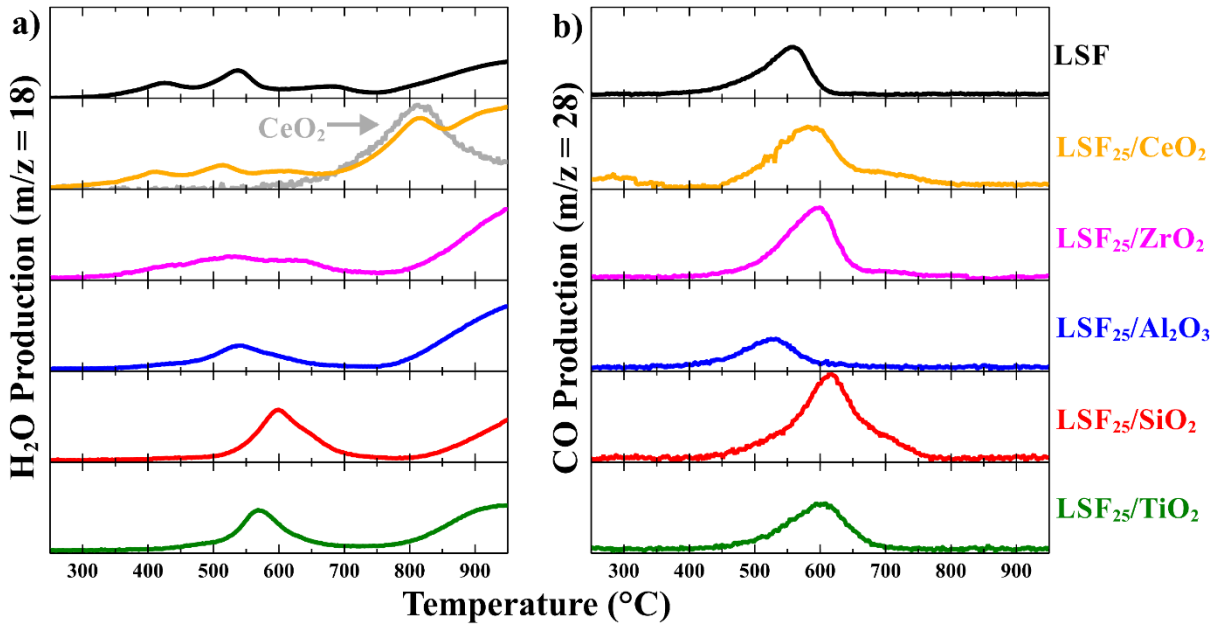

Fig. 2. a) temperature-programmed reductions with H_2 and b) temperature-programmed oxidations with CO_2 following isothermal reduction at 600 °C for LSF and affiliated composites.

production temperatures following isothermal reduction at 600 °C (Fig. 2b) undoubtedly compliment those of their respective TPRs, suggesting each of the materials are suitable for RWGS-CL.

Total H_2O and CO yields (Table 1) were obtained from numerical integration. Most notably, LSF_{25}/SiO_2 resulted in the highest H_2O and CO yields of 3690 and 1700 $\mu mol/g_{LSF}$ respectively. This significant 150% increase in CO production by LSF_{25}/SiO_2 even surpassed those of LSF_{25}/CeO_2 and LSF_{25}/ZrO_2. Due to the similarity between LSF and LSF_{25}/CeO_2 TPR profiles below 600 °C along with the CeO_2 reduction peak witnessed at about 800 °C, it was highly unlikely that this support participated in the reactions. This catalytic hindering may be alleviated by using higher redox temperatures, which contradicts the incentives for feasible CO_2 utilization due to a higher energy input. While TiO_2 appeared to have no consequential effect on the reaction, the use of Al_2O_3 is evidently detrimental to the redox properties of LSF given the 29% decrease in CO production. Nonetheless, LSF_{25}/SiO_2 remains the top composite candidate for perovskite-based syngas production.

Table 1. Quantified TPR and TPO-CO_2 results.

Sample	H_2O yield ($\mu mol/g_{LSF}$)	CO yield ($\mu mol/g_{LSF}$)
LSF	2210	690
LSF_{25}/CeO_2	1720	1100
LSF_{25}/ZrO_2	2040	1350
LSF_{25}/Al_2O_3	2920	490
LSF_{25}/SiO_2	3690	1700
LSF_{25}/TiO_2	2180	850

3.2 X-ray diffraction

XRD patterns were examined for changes in crystalline phases and the presence of secondary phases due to solid state reactions between the perovskite and support. As illustrated in Fig. 3, the overall stability of orthorhombic LSF (Ref. Code 00-035-1480) on each support is assured while (020) remains the dominant perovskite facet throughout the sample lifetime from particle sintering to the conclusion of TPO-CO_2 experiments. Rietveld refinement of the LSF diffraction pattern resulted in a Rwp value of 3.7% and RBragg of 1.0% (Fig. S2 and Table S1). The crystal structures of CeO_2, ZrO_2, Al_2O_3, SiO_2, and Al_2O_3 were cubic, monolithic, hexagonal, hexagonal, and tetragonal, respectively. Close examination revealed the minute presence of orthorhombic $FeSiO_3$ (Ref. Code 01-076-0886) and monoclinic La_2SiO_5 (Ref. Code 00-040-0234) at the LSF:SiO_2 interface following composite sintering at high temperatures. These phases have been witnessed before in iron oxide:silica composites [55] yet are not expected to exercise notable presences as reflected by current difficulties in synthesizing bulk single-phase quantities of $FeSiO_3$ [75]. In addition, cubic $Fe_{2.5}Ti_{0.5}O_4$ (Ref. Code 00-051-1587) was detected at 35.6 2θ as a result from solid state reactions during either the reduction or oxidation of LSF. These phases do not initially appear detrimental to the catalytic activity but may pose consequences of interest during the manufacturing of large-scale pellets and monoliths.

By utilizing the geometrical characteristics of the (020) diffraction line, LSF crystallite size was estimated before and after 8 cycles of RWGS-CL through a Scherrer analysis (Table 2). These values demonstrate the effect of each support on perovskite particles. By utilizing silica, the average LSF crystallite size decreases by 21% as opposed to an increase with every other support. These results compliment the expected increase in catalytic performance predicted with

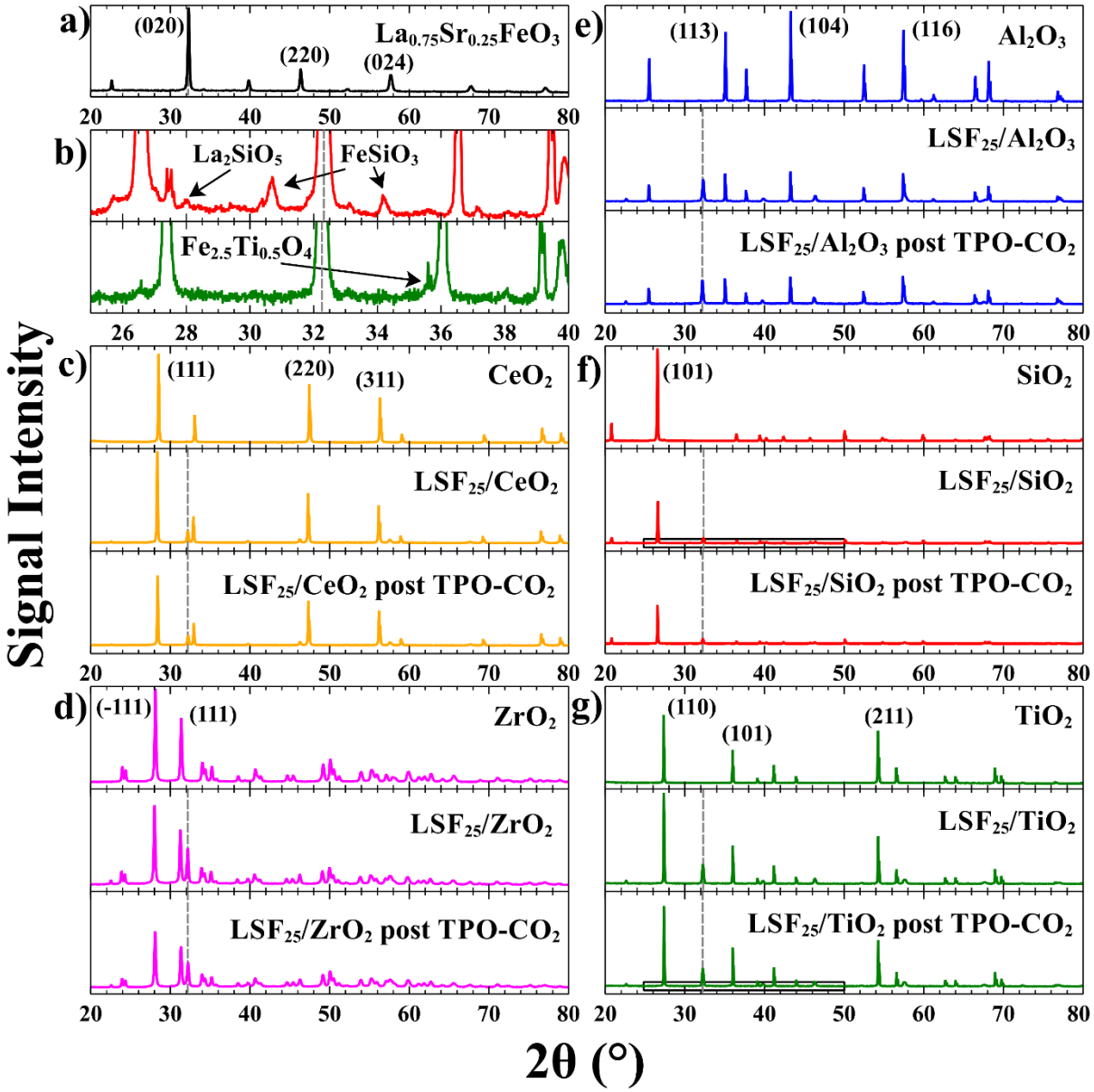

Fig. 3. Diffraction pattern of a) LSF and b) a close inspection of identified secondary phases witnessed in fresh LSF_{25}/SiO_2 (red, top) and post TPO-CO_2 LSF_{25}/TiO_2 (green, bottom). Post heat treatment at 950 °C and post TPO-CO_2 diffraction patterns of c) LSF_{25}/CeO_2, d) LSF_{25}/ZrO_2, e) LSF_{25}/Al_2O_3 (with corundum), f) LSF_{25}/SiO_2 (with quartz), and g) LSF_{25}/TiO_2 (with rutile) which all demonstrate structural stability throughout material lifetime.

Equation 1. Although the majority of the supports resulted in further sintering of the perovskite particles, they each induced strain on the perovskite lattice and enlarged the LSF cell volume. This slight expansion of interplanar distance between atoms decreases oxygen vacancy formation energy, making it easier for more oxygen to desorb from the lattice [65].

Table 2. LSF cell volume, secondary phases identified in perovskite composites, and crystallite size estimations.

Sample	LSF orthorhombic cell volume ($Å^3$)	Post – calcination secondary phases	Post - TPO-CO_2 secondary phases	Post - calcination LSF crystallite size ($Å^3$) [a]	Post – 8 cycles RWGS-CL (600 °C) LSF crystallite size ($Å^3$) [a]
LSF	237.9	-	-	370	351
LSF_{25}/CeO_2	240.5	-	-	384	526
LSF_{25}/ZrO_2	239.8	-	-	367	448
LSF_{25}/Al_2O_3	238.7	-	-	367	475
LSF_{25}/SiO_2	238.5	$FeSiO_3$, La_2SiO_5	$FeSiO_3$, La_2SiO_5	351	278
LSF_{25}/TiO_2	239.6	-	$Fe_{2.5}Ti_{0.5}O_4$	367	448

[a] *Calculated by Scherrer analysis of XRD data with a shape factor of 0.9*

3.3 DFT-based oxygen vacancy formation energies

Oxygen vacancy formation energies (E_{vac}) serve as descriptors for the ability of an oxide material to convert CO_2. If a material exhibits a high E_{vac}, it will be unwilling to form vacancies, and therefore CO_2 conversion active sites, at low RWGS-CL operating temperatures. On the other hand, a low E_{vac} will encourage numerous vacancies that are unlikely to be replenished in an oxidation reaction. With an E_{vac} of about 3.4 eV, calculated with Equation 2, LSF resides in the optimal regime for notable catalytic activity [12, 22]. Each of the supporting materials however, including CeO_2, possess E_{vac} values greater than 4.0 eV as shown in Fig. 4. These results suggests that each support remained inactive during TPO-CO_2 experiments and that the perovskite was the only phase to produce vacancies during reduction at 600 °C. Given that popular redox materials such as CeO_2 and ZrO_2 themselves do not participate in the reaction, utilizing them in low temperature RWGS-CL would contradict the investigation for a more economically friendly and kinetically enhanced composite.

Secondary phases identified through XRD analysis share unidentified roles in CO_2 conversion. Fig. 4 also includes DFT-calculated E_{vac} values for $FeSiO_3$, La_2SiO_5, and $Fe_{2.5}Ti_{0.5}O_4$ to provide insight regarding their own abilities to form oxygen vacancies at the composite interface. In regards to LSF_{25}/SiO_2, $FeSiO_3$ possesses an E_{vac} of about 5.3 eV while La_2SiO_5 resides in the much higher energy regime with an E_{vac} of about 7.0 eV. Given that CeO_2, the oxide with the lowest E_{vac} aside from LSF, did not form its own vacancies until about 700 °C in the TPR experiments, it remains highly improbable that these secondary phases are active participants at these experimental temperatures. The same conclusion was reached for $Fe_{2.5}Ti_{0.5}O_4$ due to its relatively high E_{vac} of about 6.0 eV.

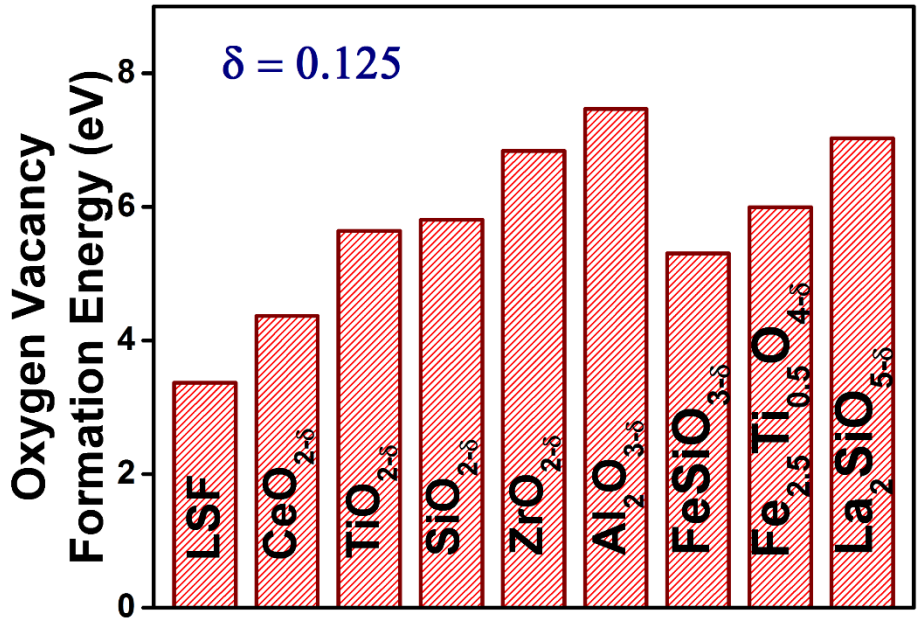

Fig. 4. DFT-calculated oxygen vacancy formation energies of LSF, supporting materials, and detected secondary phases. δ represents the extent of oxygen nonstoichiometry for each support

3.4 Microscopy

Detailed images of each composite following 8 cycles of RWGS-CL are arranged in Fig. 5. TEM revealed a consistent interplanar spacing of 0.27 Å for the LSF (020) facet when combined with each support. Minor amounts of strain resulted at each perovskite:support site of contact due to both interfacial forces and cationic migration during solid state reactions at high temperatures. The interplanar spacings of the LSF (020) facet on CeO_2, ZrO_2, Al_2O_3, SiO_2, and TiO_2 are 2.86, 2.74, 2.74, 2.78, and 2.70 Å respectively. The repercussions of this expanded lattice include decreased oxygen vacancy formation energy by perovskites and increased cell volume in accordance with XRD data.

The SEM images however provided valuable insight to changes in CO_2 conversion by LSF. The CeO_2, ZrO_2, and SiO_2 supports form small particles which correspond to the high CO yields in the TPO-CO_2 experiments. SiO_2 in particular demonstrated the greatest reduction in perovskite particle size, especially in comparison to the abundant alternatives. SEM also emphasized distinction between different oxide morphologies, e.g. orthorhombic perovskite particles and hexagonal Al_2O_3 plates. Not only did LSF retain its size, but hexagonal Al_2O_3 plates and TiO_2 growth appeared to be supported on, if not masking, the perovskite as seen in Fig. 5e and 5i, respectively. This encapsulation explains the absence of kinetic enhancement when using Al_2O_3 and TiO_2 as supports with physical barriers hindering CO_2 adsorption to the perovskite surface.

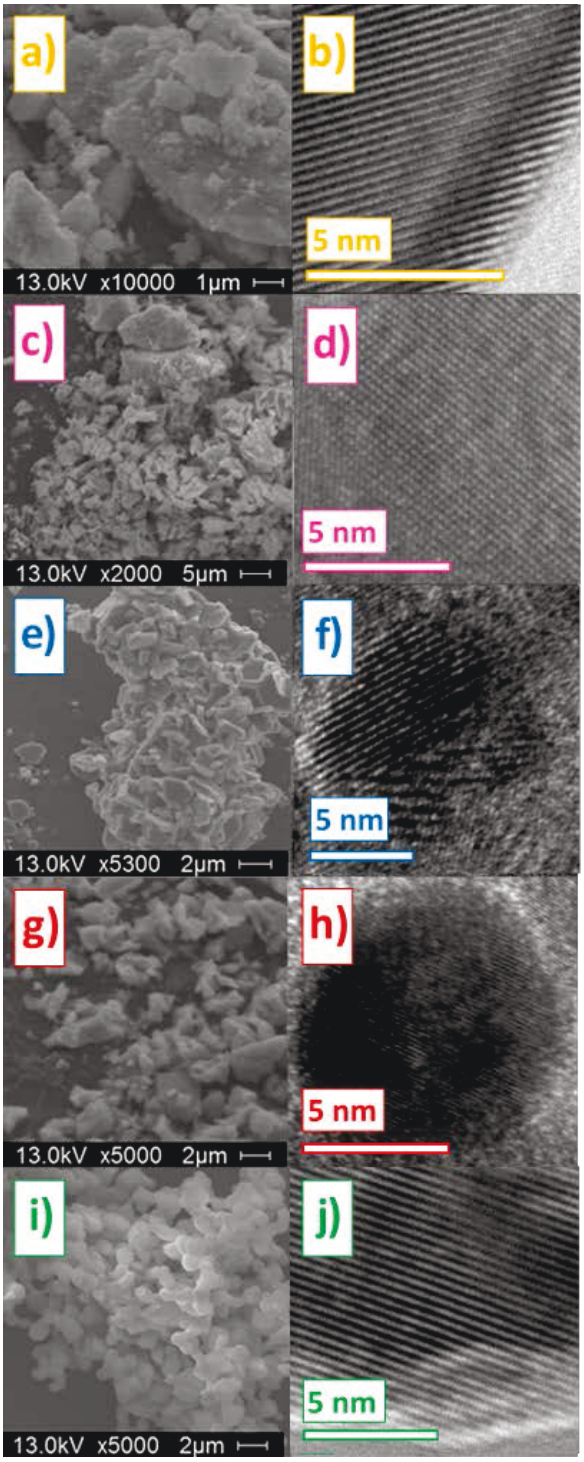

Fig. 5. SEM and TEM images respectively of a-b) LSF_{25}/CeO_2, c-d) LSF_{25}/ZrO_2, e-f) LSF_{25}/Al_2O_3, g-h) LSF_{25}/SiO_2, and i-j) LSF_{25}/TiO_2 all after 8 cycles of the RWGS-CL process at 600 °C

4.0 Discussion

Given the array of supports tested, SiO_2 enhanced the redox properties of LSF to achieve a CO yield of 1700 μmol/g_{LSF}, far beyond what was accomplished by CeO_2 or ZrO_2. This was in part due to the material's ability to restructure the perovskite oxide into smaller particles capable of quicker oxygen exchange. Not only is this phenomenon expected to work for any perovskite formulation, but it may be further improved with greater support porosity using related alternatives such as SBA-15, a form of mesoporous SiO_2 [76, 77]. Although some secondary phase formation with the use of silica occurred, its use yields less cationic exchange between phases than other supports presumably would. As demonstrated in this study, the RWGS-CL process may be operated at temperatures low enough to maintain both large SiO_2 pores [78] and small perovskite particles. X-ray photoelectron spectrometry results (Fig. S3) suggest that the type of oxide support does not pose a significant effect on the Fe^{3+}/Fe^{2+} surface content ratio.

The secondary phases that accompany these supported perovskites (Table 2) may potentially offset the enhancements observed in this study if generated out of proportion. Single-phase bulk synthesis of impurities identified in LSF_{25}/SiO_2 such as $FeSiO_3$ and La_2SiO_5 comes with great thermodynamic challenges [75] and often appear in other material syntheses in trace quantities [79, 80]. This exacerbates the difficulty in studying these materials and their contribution to chemical looping. Impurities such as $FeSiO_3$ and La_2SiO_5 exhibit high oxygen vacancy formation energy in relation to perovskite oxides (Fig. 4) and, therefore, are speculated to possess no beneficial qualities for oxygen exchange and transport. As delineated by Hubbard and Scholm, the mixing of SiO_2 and one of various transition metal oxides may lead to the spontaneous formation of several secondary phases at elevated temperatures [81]. These reactions with perovskites in particular are aided by the effluent migration of cationic metals (Fe

and La in this case) to the material surface during reduction at high temperature [82, 83]. These surface cations then diffuse onto SiO_2 [84] to form secondary phases, converting the perovskite oxide into its non-stoichiometric forms. Maiti et. al computationally demonstrated an increase in E_{vac} for defect-laden perovskite oxides [22]. This seems to be in agreement with the small elevation in reduction temperature noted for both LSF_{25}/SiO_2 and LSF_{25}/TiO_2. Although seemingly inevitable when combined with SiO_2, the kinetic deconstruction of perovskite oxides and formation of secondary phases at the composite interface may be minimized or potentially avoided completely by maintaining low sintering and reaction temperatures. This was suggested by the early appearance of $FeSiO_3$ and La_2SiO_5 observed after subjecting the mixed powders to thermal treatment and their increased presence after TPO-CO_2 experiments conducted up to 950 °C.

Encapsulation of perovskites by Al_2O_3 and TiO_2 over time is detrimental to CO_2 conversion. These oxide shells accounted for zero and negative changes in CO production in TPO-CO_2 experiments due to the barrier between gaseous CO_2 and kinetic exchange sites on the perovskite surface. Because vacancy formation in these supporting materials is highly improbable, according to Fig. 4, CO_2 adsorption strength will be relatively weak [12] and transport restrictions will severely limit catalyst efficiency. These results match the findings of Kharton et al. who observed a decrease in oxygen permeation fluxes through perovskites-based composites that consist of Al_2O_3 and even $SrAl_2O_4$ [52], the latter of which was not discerned in this study. It is therefore recommended to design SiO_2-based frameworks that maintain high surface area and structural stability for long-term redox chemical looping.

5.0 Conclusion

This study addressed the factors that currently limit perovskite oxide utilization for solar-driven CO_2 conversion through the reverse water-gas shift chemical looping process. The use of SiO_2 as a support significantly reduced $La_{0.75}Sr_{0.25}FeO_3$ crystallite size and the extent of oxygen self-diffusion retardation. This resulted in a CO yield of 1700 μmol/g_{LSF}, 150% greater than the control sample. Slight interfacial formation of secondary phases $FeSiO_3$ and La_2SiO_5, detected by X-ray diffraction, was negligible but may pose severe consequences to catalyst efficiency if the solid-state kinetics are not restricted with low synthesis and operation temperatures. This result was due to the high oxygen vacancy formation energies of these phases which originated from the deconstruction of the perovskite phase at the interface. Nevertheless, SiO_2 outperformed other supporting materials of interest including CeO_2 and ZrO_2 which demonstrated no activity at the low experiment temperatures. Abundant alternatives such as Al_2O_3 and TiO_2 encapsulated the perovskite particles, therefore hindering CO_2 adsorption to surface vacancies. The effects of using various supports for feasible syngas production has been demonstrated and the reasoning behind such material enhancement has been described.

Acknowledgements

The authors congratulate Professor Umit S. Ozkan for winning the 2017 Henry H. Storch Award in Fuel Science, given by the ACS Division of Energy & Fuels. NSF grants CBET-1335817, IIP-1743623, CHE-1531590, and EEC-1560303, the NASA Florida Space Grant Consortium Masters Fellowship (to BJH), and the USF Office of Graduate Studies Dissertation Completion Fellowship (to DM) are gratefully acknowledged for funding. Thanks goes to Dr. Lukasz Wojtas for assistance with Rietveld refinement of XRD patterns and Dr. Anne Meier for assistance with XPS data acquisition. The authors of this project would like to recognize the USF

Nanotechnology Research and Education Center for imaging assistance and resources along with the Research Computing, USF for computational resources.

Declaration of Interest:

A provisional patent has been filed by USF on related technology.

References

[1] M. Mobilia, Even as renewables increase, fossil fuels continue to dominate U.S. energy mix, in: I.S. Analysis (Ed.), 2017.
[2] U.S. Energy-Related Carbon Dioxide Emissions, 2016, in: I.S. Analysis (Ed.), 2017.
[3] I. Wender, Reactions of synthesis gas, Fuel Process. Technol., 48 (1996) 189-297.
[4] R.L. Pruett, Industrial organic chemicals through utilization of synthesis gas, Ann. N. Y. Acad. Sci., 295 (1977) 239-248.
[5] Chemicals from Synthesis Gas: Catalytic Reactions of CO and H_2, D. Reidel Publishing Company, Dordrecht, Holland, 1983.
[6] Hydrocarbon Gas Liquids (HGL): Recent Market Trends and Issues, I.S. Analysis, U.S. Energy Information Adminsitration (2014).
[7] Y.A. Daza, R.A. Kent, M.M. Yung, J.N. Kuhn, Carbon dioxide conversion by reverse water gas shift chemical looping on perovskite-type oxides, Ind. Eng. Chem. Res., 53 (2014) 5828-5837.
[8] Y.A. Daza, J.N. Kuhn, CO_2 conversion by reverse water gas shift catalysis: comparison of catalysts, mechanisms, and their consequences for CO_2 conversion to liquid fuels, RSC Adv., 6 (2016) 49675-49691.
[9] P. Kaiser, R.B. Unde, C. Kern, A. Jess, Production of Liquid Hydrocarbons with CO_2 as Carbon Source based on Reverse Water-Gas Shift and Fischer-Tropsch Synthesis, Chem. Ing. Tech., 85 (2013) 489-499.
[10] M.G. Walter, E.L. Warren, J.R. McKone, S.W. Boettcher, Q. Mi, E.A. Santori, N.S. Lewis, Solar Water Splitting Cells, Chem. Rev., 110 (2010) 6446-6473.
[11] Y.A. Daza, D. Maiti, B.J. Hare, V.R. Bhethanabotla, J.N. Kuhn, More Cu, more problems: Decreased CO_2 conversion ability by Cu-doped $La_{0.75}Sr_{0.25}FeO_3$ perovskite oxides, Surf. Sci., 648 (2016) 92-99.
[12] Y.A. Daza, D. Maiti, R.A. Kent, V.R. Bhethanabotla, J.N. Kuhn, Isothermal reverse water gas shift chemical looping on $La_{0.75}Sr_{0.25}Co_{(1-Y)}Fe_YO_3$ perovskite type oxides, Catal. Tod., 258 (2015) 691-698.
[13] M. Wenzel, L. Rihko-Struckmann, Thermodynamic Analysis and Optimization of RWGS Processes for Solar Syngas Production from CO_2, AIChE J., 63 (2017) 15-22.
[14] D.S. Mallapragada, N.R. Singh, V. Curteanu, R. Agrawal, Sun-to-Fuel Assessment of Routes for Fixing CO_2 as Liquid Fuel, Ind. Eng. Chem. Res., 52 (2013) 5136-5144.
[15] M.A. Peña, J.L.G. Fierro, Chemical Structures and Performance of Perovskite Oxides, Chem. Rev., 101 (2001) 1981-2017.
[16] D. Maiti, B.J. Hare, Y.A. Daza, A.E. Ramos, J.N. Kuhn, V.R. Bhethanabotla, Earth Abundant Perovskite Oxides for Low Temperature CO_2 Conversion, Energy Environ. Sci., 11 (2018) 648-659.

[17] A. Demont, S. Abanades, E. Beche, Investigation of Perovskite Structures as Oxygen-Exchange Redox Materials for Hydrogen Production from Thermochemical Two-Step Water-Splitting Cycles, J. Phys. Chem. C, 118 (2014) 12682-12692.
[18] A. Evdou, V. Zaspalis, L. Nalbandian, $La_{1-x}Sr_xFeO_{3-\delta}$ perovskites as redox materials for application in a membrane reactor for simultaneous production of pure hydrogen and synthesis gas, Fuel, 89 (2010) 1265-1273.
[19] A.H. McDaniel, A. Ambrosini, E.N. Coker, J.E. Miller, W.C. Chueh, R. O'Hayre, J. Tong, Nonstoichiometric perovskite oxides for solar thermochemical H_2 and CO production, Energy Procedia, 49 (2014) 2009-2018.
[20] S. Carter, A. Selcuk, R.J. Chater, J. Kajada, J.A. Kilner, B.C.H. Steele, Oxygen transport in selected nonstoichiometric perovskite-structure oxides, 53-56 (1992) 597.
[21] M. Søgaard, P.V. Hendriksen, M. Mogensen, Oxygen nonstoichiometry and transport properties of strontium substituted lanthanum ferrite, J. Solid State Chem., 180 (2007) 1489-1503.
[22] D. Maiti, Y.A. Daza, M.M. Yung, J.N. Kuhn, V.R. Bhethanabotla, Oxygen vacancy formation characteristics in the bulk and across different surface terminations of $La_{(1-x)}Sr_xFe_{(1-y)}Co_yO_{(3-\delta)}$ perovskite oxides for CO_2 conversion, J. Mater. Chem. A, 4 (2016) 5137-5148.
[23] L. Nalbandian, A. Evdou, V. Zaspalis, $La_{1-x}Sr_xMO_3$ (M = Mn, Fe) perovskites as materials for thermochemical hydrogen production in conventional and membrane reactors, Int. J. Hydrogen Energy, 34 (2009) 7162-7172.
[24] G.W. Coffey, J.S. Hardy, L.R. Pederson, P.C. Rieke, E.C. Thomsen, Oxygen Reduction Activity of Lanthanum Strontium Nickel Ferrite, Electrochem. and Solid-State Lett., 6 (2003) A121-A124.
[25] E.V. Tsipis, M.V. Patrakeev, V.V. Kharton, A.A. Yaremchenko, G.C. Mather, A.L. Shaula, I.A. Leonidov, V.L. Kozhevnikov, J.R. Frade, Transport properties and thermal expansion of Ti-substituted $La_{1-x}Sr_xFeO_{3-\delta}$ (x = 0.5-0.7), Solid State Sci., 7 (2005) 355-365.
[26] L.M. Neal, A. Shafiefarhood, F. Li, Dynamic Methane Partial Oxidation Using a Fe_2O_3@$La_{0.8}Sr_{0.2}FeO_{3-\delta}$ Core–Shell Redox Catalyst in the Absence of Gaseous Oxygen, ACS Catal., 4 (2014) 3560-3569.
[27] S. Furfori, S. Bensaid, N. Russo, D. Fino, Towards practical application of lanthanum ferrite catalysts for NO reduction with H_2, Chem. Eng. J., 154 (2009) 348-354.
[28] Advances in Clean Hydrocarbon Fuel Processing: Science and Technology, Woodhead Publishing, Cambridge, UK, 2011.
[29] C. Agrafiotis, M. Roeb, C. Sattler, A review on solar thermal syngas production via redox pair-based water/carbon dioxide splitting thermochemical cycles, Renewable Sustainable Energy Rev., 42 (2015) 254-285.
[30] P. Furler, J.R. Scheffe, A. Steinfeld, Syngas production by simultaneous spliting of H2O and CO2 via ceria redox reactions in a high-temperature solar reactor, Energy Environ. Sci., 5 (2012) 6098-6103.
[31] E. Gallei, E. Schwab, Development of technical catalysts, Catal. Today, 51 (1999) 535-546.
[32] M. Campanati, G. Fornasari, A. Vaccari, Fundamentals in the preparation of heterogeneous catalysts, Catal. Today, 77 (2003) 299-314.
[33] A.T. Bell, The Impact of Nanoscience on Heterogeneous Catalysis, Science, 299 (2003) 1688-1691.
[34] J. Maier, On the correlation of macroscopic and microscopic rate constants in solid state chemistry, Solid State Ionics, 112 (1998) 197-228.

[35] R. Bredesen, F. Mertins, T. Norby, Measurements of surface exchange kinetics and chemical diffusion in dense oxygen selective membranes, Catal. Today, 56 (2000) 315-324.
[36] E.N. Armstrong, K.L. Duncan, E.D. Wachsman, Effect of A and B-site cations on surface exchange coefficient for ABO_3 perovskite materials, Phys. Chem. Chem. Phys., 15 (2013) 2298-2308.
[37] H.J.M. Bouwmeester, H. Kruidhof, A.J. Burggraaf, Importance of the surface exchange kinetics as rate limiting step in oxygen permeation through mixed-conducting oxides, Solid State Ionics, 72 (1994) 185.
[38] J. Crank, The mathematics of diffusion, 2nd. ed., Oxford University Press, Oxford, England, 1979.
[39] Y.D. Bi, W. Zhang, H.Y. Xu, W.Z. Li, Nanocrystalline CeO2 in SBA-15: Performance of Pt/CeO2/SBA-15 Catalyst for Water-gas-shift Reaction, 119 (2007) 126-133.
[40] P. Concepcion, A. Corma, J. Silvestre-Albero, CeO2-doped nanostructured materials as a support of Pt catalysts: chemoselective hydrogenation of crotonaldehyde, 46 (2007) 31-38.
[41] V.V. Galvita, H. Poelman, V. Bliznuk, C. Detavernier, G.B. Marin, CeO_2- Modified Fe_2O_3 for CO_2 Utilization via Chemical Looping, Ind. Eng. Chem. Res., 52 (2013) 8416−8426.
[42] A. Goguet, F. Meunier, J.P. Breen, R. Burch, M.I. Petch, A.F. Ghenciu, Study of the origin of the deactivation of a Pt/CeO_2 catalyst during reverse water gas shift (RWGS) reaction, J. Catal., 226 (2004) 382-392.
[43] A. Goguet, F.C. Meunier, D. Tibiletti, J.P. Breen, R. Burch, Spectrokinetic Investigation of Reverse Water-Gas Shift Reaction Intermediates over a Pt/CeO_2 Catalyst, J. Phys. Chem. B, 108 (2004) 20240-20246.
[44] G. Jacobs, L. Williams, U. Graham, D. Sparks, B.H. Davis, Low-Temperature Water-Gas Shift: In-Situ DRIFTS-Reaction Study of a Pt/CeO_2 Catalyst for Fuel Cell Reformer Applications, J. Phys. Chem. B, 107 (2003) 10398-10404.
[45] L. Wang, S. Zhang, Y. Liu, Reverse water gas shift reaction over Co-precipitated Ni-CeO_2 catalysts, J. Rare Earth, 26 (2008) 66-70.
[46] T. Zhu, M. Flytzani-Stephanopoulos, Catalytic partial oxidation of methane to synthesis gas over Ni–CeO2, 208 (2001) 403.
[47] K. Sayama, H. Arakawa, Photocatalytic Decomposition of Water and Photocatalytic Reduction of Carbon Dioxide over ZrO2 Catalyst, J. Phys. Chem., 97 (1993) 531-533.
[48] T. Yamaguchi, Application of ZrO_2 as a catalyst and a catalyst support, Catal. Today, 20 (1994) 199-217.
[49] O.H. Laguna, F.R. Sarria, M.A. Centeno, J.A. Odriozola, Gold supported on metal-doped ceria catalysts (M = Zr, Zn, and Fe) for the preferential oxidation of CO (PROX), J. Catal., 276 (2010) 360-370.
[50] J. Tong, Q. Jiang, Z. Chen, Z. Jiang, C. Li, Two-step thermochemical cycles for CO_2 splitting on Zr-doped cobalt ferrite supported on silica, Sol. Energy, 116 (2015) 133-143.
[51] M.M. Pakulska, C.M. Grgicak, J.B. Giorgi, The effect of metal and support particle size on NiO/CeO2 and NiO/ZrO2 catalyst activity in complete methane oxidation, 332 (2007) 124-129.
[52] V.V. Kharton, A.L. Shaula, F.M.M. Snijkers, J.F.C. Cooymans, J.J. Luyten, I.P. Marozau, A.P. Viskup, F.M.B. Marques, J.R. Frade, Oxygen transport properties in ferrite-based ceramic membranes: Effects of alumina sintering aid, J. Eur. Ceram. Soc., 26 (2006) 3695-3704.
[53] H. Pines, W.O. Haag, Alumina: Catalyst and Support. I. Alumina, its Intrinsic Acidity and Catalytic Activity, J. Am. Chem. Soc., 82 (1960) 2471-2483.

[54] R.W. Hicks, N.B. Castagnola, Z. Zhang, T.J. Pinnavaia, C.L. Marshall, Lathlike mesostructured γ-alumina as a hydrodesulfurization catalyst support, Appl. Catal., A, 254 (2003) 311-317.
[55] Q. Jiang, J. Tong, G. Zhou, Z. Jiang, Z. Li, C. Li, Thermochemical CO_2 splitting reaction with supported $La_xA_{1-x}Fe_yB_{1-y}O_3$ (A = Sr, Cr, B = Co, Mn; $0 \leq x, y \leq 1$) perovskite oxides, Sol. Energy, 103 (2014) 425-437.
[56] T. Fujikawa, K. Idei, T. Ebihara, H. Mizuguchi, K. Usui, Aromatic hydrogenation of distillates over SiO2-Al2O3-supported noble metal catalysts, 192 (2000) 253-261.
[57] S.R. Kirumakki, B.G. Shpeizer, G.V. Sagar, K.V.R. Chary, A. Clearfield, Hydrogenation of Naphthalene over $NiO/SiO_2–Al_2O_3$ catalysts: Structure–activity correlation, 242 (2006) 319.
[58] S. Lecarpentier, J. van Gestel, K. Thomas, J.-P. Gilson, M. Houalla, Study of Ir/WO3/ZrO2–SiO2 ring-opening catalysts: Part II. Reaction network, kinetic studies and structure–activity correlation, 254 (2008) 49-63.
[59] G. Wan, A. Duan, Z. Zhao, G. Jiang, D. Zhang, R. Li, T. Dou, K.H. Chung, Al_2O_3-TiO_2/Al_2O_3-TiO_2-SiO_2 Composite-Supported Bimetallic Pt-Pd Catalysts for the Hydrodearomatization and Hydrodesulfurization of Diesel Fuel 23 (2009) 81-85.
[60] S.S. Kim, H.H. Lee, S.C. Hong, The effect of the morphological characteristics of TiO_2 supports on the reverse water–gas shift reaction over Pt/TiO_2 catalysts, Appl. Catal. B: Environ., 119-120 (2012) 100-108.
[61] P. Panagiotopoulou, D.I. Kondarides, X.E. Verykios, Mechanistic aspects of the selective methanation of CO over Ru/TiO_2 catalyst, Catal. Today, 181 (2012) 138-147.
[62] M. Popa, M. Kakihana, Synthesis of lanthanum cobaltite ($LaCoO_3$) by the polymerizable complex route, Solid State Ionics, 151 (2002) 251-257.
[63] S. Ivanova, A. Senysshyn, E. Zhecheva, K. Tenchev, V. Nikolov, R. Stoyanova, H. Fuess, Effect of the synthesis route on the microstructure and the reducibility of $LaCoO_3$, J. Alloys Compd., 480 (2009) 279-285.
[64] W.W. Wendlandt, The thermolysis of the rare earth and other metal nitrates, Anal. Chim. Acta, 15 (1956) 435-439.
[65] B.J. Hare, D. Maiti, Y.A. Daza, V.R. Bhethanabotla, J.N. Kuhn, Enhanced CO_2 conversion to CO by silica supported perovskite oxides at low temperatures, ACS Catal., 8 (2018) 3021-3029.
[66] B.D. Cullity, Elements of X-Ray Diffraction, Addison-Wesley Publishing Company, Inc., USA, 1956.
[67] S.E. Dann, D.B. Currie, M.T. Weller, The Effect of Oxygen Stoichiometry on Phase Relations and Structure in the System $La_{1-x}Sr_xFeO_{3-\delta}$ ($0 \leq x \leq 1$, $0 \leq \delta \leq 0.5$), J. Solid State Chem., 109 (1994) 134-144.
[68] P. Hohenberg, W. Kohn, Inhomogeneous Electron Gas, Phys. Rev., 136 (1964) B864-B871.
[69] W. Kohn, L.J. Sham, Self-Consistent Equations Including Exchange and Correlation Effects, Phys. Rev., 140 (1965) A1133-A1138.
[70] G. Kresse, J. Furthmüller, Efficiency of ab-initio total energy calculations for metals and semiconductors using a plane-wave basis set, Comput. Mater. Sci., 6 (1996) 15-50.
[71] G. Kresse, D. Joubert, From ultrasoft pseudopotentials to the projector augmented-wave method, Phys. Rev. B, 59 (1999) 1758-1775.
[72] J.P. Perdew, K. Burke, M. Ernzerhof, Generalized Gradient Approximation Made Simple, 77 (1996) 3865-3868.

[73] H.J. Monkhorst, J.D. Pack, Special points for Brillouin-zone integrations, Phys. Rev. B, 13 (1976) 5188-5192.
[74] L. Wang, T. Maxisch, G. Ceder, Oxidation energies of transition metal oxides within the GGA + U framework, Phys. Rev. B, 73 (2006) 195107.
[75] D.H. Lindsley, B.T.C. Davis, I.D. MacGregor, Ferrosilite ($FeSiO_3$): Synthesis at High Pressures and Temperatures, Science, 144 (1964) 73-74.
[76] A. Katiyar, S. Yadav, P.G. Smirniotis, N.G. Pinto, Synthesis of ordered large pore SBA-15 spherical particles for adsorption of biomolecules, J. Chromatogr. A, 1122 (2006) 13-20.
[77] D. Zhao, J. Feng, Q. Huo, N. Melosh, G.H. Fredrickson, B.F. Chmelka, G.D. Stucky, Triblock Copolymer Syntheses of Mesoporous Silica with Periodic 50 to 300 Angstrom Pores, Science, 279 (1998) 548-552.
[78] M. Kruk, M. Jaroniec, Characterization of the Porous Structure of SBA-15, Chem. Mater., 12 (2000) 1961-1968.
[79] S. Tao, J.T.S. Irvine, Preparation and characterization of apatite-type lanthanum silicates by a sol-gel process, Mater. Res. Bull., 36 (2001) 1245-1258.
[80] Y. Zhou, K. Hirao, K. Watari, Y. Yamauchi, S. Kanzaki, Thermal conductivity of silicon carbide densified with rare-earth oxide additives, J. Eur. Ceram. Soc., 24 (2004) 265-270.
[81] K.J. Hubbard, D.G. Schlom, Thermodynamic stability of binary oxides in contact with silicon, J. Mater. Res., 11 (1996) 2757-2776.
[82] Y. Nishihata, J. Mizuki, T. Akao, H. Tanaka, M. Uenishi, M. Kimura, T. Okamoto, N. Hamada, Self-regeneration of a Pd-perovskite catalyst for automotive emissions control, Nature, 418 (2002) 164-167.
[83] P. Ciambelli, S. Cimino, L. Lisi, M. Faticanti, G. Minelli, I. Pettiti, P. Porta, La, Ca, Fe oxide perovskites: preparation, characterization and catalytic properties for methane combustion, Appl. Catal., B, 33 (2001) 193-203.
[84] B.K. Min, A.K. Santra, D.W. Goodman, Understanding silica-supported metal catalysts: Pd/silica as a case study, Catal. Today, 85 (2003) 113-124.